Mechanics of Materials 191 (2024) 104951

Contents lists available at ScienceDirect

Mechanics of Materials

journal homepage: www.elsevier.com/locate/mechmat

Editor-in-Chief Invited Article

Mechanical properties and deformation mechanisms of single crystal Mg micropillars subjected to high-strain-rate C-axis compression

Z. Lin [a], D.J. Magagnosc [b], J. Wen [c], X. Hu [d], H.D. Espinosa [a,e,*]

[a] Theoretical and Applied Mechanics, Northwestern University, 2145 Sheridan Road, Evanston, IL, 60208, USA
[b] DEVCOM Army Research Laboratory, Aberdeen Proving Ground, Aberdeen, MD, 21005, USA
[c] Argonne National Lab, 9700 S. Cass Avenue, Lemont, IL, 60439, USA
[d] Department of Materials Science and Engineering, Northwestern University, Evanston, IL, 60208, USA
[e] Department of Mechanical Engineering, Northwestern University, 2145 Sheridan Road, Evanston, IL, 60208, USA

ARTICLE INFO

Keywords:
In situ SEM
Magnesium
Compression
Micropillar
Strain rate effect

ABSTRACT

The mechanical properties and deformation mechanisms of single crystal magnesium under c-axis quasi-static and high-strain rate compressions are investigated through *in situ* scanning electron microscope (SEM) experiments and post-mortem transmission electron microscope (TEM) characterization. The findings revealed that ductility and high rates of hardening are preserved for pillars as large as 15 μm. Furthermore, rate effects result in a mild increase in flow stress with plastic deformations controlled primarily by the slip of <a+c> type dislocations. Importantly and in contrast to other literature reports, plastic deformation occurs in the *absence of twining*. As the strain increases and plastic deformation exceeds about 4%, crystal rotation activates basal slip, <a> type dislocations, resulting in a more rate independent flow stress. TEM observation on micropillars compressed at a strain rate of 250/s, revealed the activation of $\{11\bar{2}2\}\langle\bar{1}\bar{1}23>$ slip systems and high mobility of screw dislocations as major contributors to plastic strains in excess of 10% *without fracture*. These findings are relevant to the design of lightweight materials used in transportation systems, e.g., selection of material grain size. Moreover, the experimental data here reported provides the materials science community with a unique opportunity to validate discrete dislocation dynamics (DDD) formulations employed in multiscale design of materials.

1. Introduction

Magnesium (Mg) and its alloys have long attracted much interest due to their low density and the resulting high strength-to-density ratio, making them desirable as structural materials for transportation applications (Dziubińska et al., 2016; Joost and Krajewski, 2017; Klaumünzer et al., 2019). However, their usage is hampered by low formability due to the limited number of slip systems available in Mg, in addition to other factors such as vulnerability to corrosion and low creep resistance. Moreover, magnesium's limited ductility and propensity for cracking present design challenges, e.g., safety in the event of road collisions. These challenges have motivated researchers to better understand the mechanical properties and deformation mechanisms of Mg as a function of size and strain rate.

Magnesium's limited ductility and processability are due to the limited number of independent crystallographic slip systems. It is known that a minimum of five independent slip systems are required for arbitrary and homogeneous deformation (Mises, 1928; Taylor, 1938). Early studies (Burke and Hibbard, 1952; Conrad and Robertson, 1957; Yoshinaga and Horiuchi, 1963; Roberts, 1960) on deformation mechanisms in single crystal Mg revealed two basal slip systems, i.e., slip of dislocations with $\frac{1}{3}<11\bar{2}0>$ (or $<a>$) type Burgers vectors within the (0001) basal plane. The slip of <a> type dislocations are also observed on prismatic $\{10\bar{1}0\}$ (Flynn et al., 1961; Quimby et al., 1962) and pyramidal $\{10\bar{1}1\}$ (Reed-Hill and Robertson, 1957a; Reedhill and Robertson, 1958) planes. Collectively these slip systems result in a total of four independent slip modes. Critically, none of these slip systems can accommodate deformation along the c-axis.

In bulk, deformation twinning during c-axis tension (Yoshinaga and Horiuchi, 1963; Reed-Hill and Robertson, 1957b) and compression (Reed-Hill and Robertson, 1957b; Chapuis and Driver, 2011; Yoshinaga et al., 1973) is a potential source for plasticity. Unfortunately, twinning

* Corresponding author. Theoretical and Applied Mechanics, Northwestern University, 2145 Sheridan Road, Evanston, IL, 60208, USA.
E-mail address: espinosa@northwestern.edu (H.D. Espinosa).

https://doi.org/10.1016/j.mechmat.2024.104951
Received 23 September 2023; Received in revised form 24 January 2024; Accepted 13 February 2024
Available online 16 February 2024

introduces localization and potential crack initiation sites leading to fracture. An alternative mechanism to achieve arbitrary deformation should come from slip systems whose Burgers vectors contain a <c>-axis component, e.g., the $\{11\overline{2}\overline{2}\}\langle\overline{1}\overline{1}23>$ (or pyramidal II <a+c>) slip system is one such system (Stohr and Poirier, 1972; Obara et al., 1973) and the most reported activated system during c-axis compression in Mg. However, this mechanism is not always present in experiments (Byer et al., 2010; Byer and Ramesh, 2013) or molecular dynamic simulations (Li and Ma, 2009). Indeed, high fidelity molecular dynamic studies revealed that basal dissociation of <a+c> dislocation into sessile low energy <a+c> and <c> partials are the root-cause of low ductility (Wu and Curtin, 2015; Wu et al., 2018) As pointed out by Curtin and co-workers, the dissociation process is temperature and rate dependent, hence <a+c> sliding can occur over certain distances before dissociation into immobile dislocations occurs. This elicits the need to investigate the effect of size on pure Mg plasticity and raises questions about what conditions necessitate pyramidal II slip.

In an ideal c-axis compression test, any of the slip systems with solely <a> or <c> type Burgers vector would have a Schmid factor of 0. Therefore, any significant amount of plasticity would necessitate pyramidal II slip. However, due to the very small critical resolved shear stress (CRSS) of basal slip (0.5 MPa), (Burke and Hibbard, 1952; Conrad and Robertson, 1957; Yoshinaga and Horiuchi, 1963) compared to 40 MPa (Obara et al., 1973) for pyramidal II <a+c>, implies that a tiny misalignment could lead to the activation of basal slip. This feature can be seen in Fig. 1, where the minimum normal stress, σ_{min}, required for the activation of basal slip and pyramidal II <a+c> slip, is plotted as a function of the misalignment from the c-axis. σ_{min} is given by

$$\sigma \bullet m(\theta) \geq \text{CRSS}$$

where σ is the compressive stress on a plane perpendicular to the loading direction, m is the Schimd factor for a given slip system, which is a function of the angle, θ, between the loading direction and the c-axis. Note that a misalignment as small as 0.4° would make basal slip more favourable than pyramidal II slip. Indeed, Wonsiewicz (1966) reported an angle as small as 0.15° for basal slip activation. Activation of basal slip in c-axis compressed Mg micropillars was observed (see for example Fig. 2c in (Lilleodden, 2010) or Fig. 4 in Byer and Ramesh, 2013), which reveals the experimental challenge.

Obara et al. (1973) reported extensive TEM characterization on bulk single crystal Mg loaded along the c-axis, where all three types of dislocations, i.e., <a>, <c> and <a+c>, were found in the samples. They attributed the plasticity to the <a+c> type dislocations. The <c> type dislocations were considered a result of a reaction between an <a+c> dislocation and an <a> dislocation on the basal plane. Ando et al. (2010) reported activity of pyramidal II slip systems in c-axis compression, but the crystal fractured at around 1% strain due to double twinning, suggesting very limited slip activity. *In situ* TEM compression tests revealed either $\{10\overline{1}1\}$ contraction twins (Yu et al., 2012) or pyramidal II slip (Liu et al., 2019) as deformation mechanisms to achieve very high strains. However, these experiments were on nanoscale pillars where there is scarcity of dislocations and a large surface area for dislocations to escape. This begs the question, is the observed plasticity the result of tests conducted on submicron pillars or a more general size scale effect that can be used more broadly in applications involving materials with micron size grains?

A review of the literature reveals that <a>-axis compression studies are the most abundant because they promote tension twinning. Compression along the c-axis is much less explored, especially in micron size single crystals and at higher strain rates, in the range of 0.1 s^{-1} to 10^3 s^{-1}, which are most relevant in transportation collisions. Li reported high strain rate compression tests, via split Hopkinson bar experiments, on single crystal Mg, (Li, 2011, 2013) up to a strain rate of 1200/s. Unlike other studies intended to investigate the c-axis compression behavior, the loading direction deviates from the c-axis by 10°. Surprisingly, the pyramidal II slip systems were still activated, though the sample fractured along the slip planes at around 6% strain.

These experiments suggest that the deformation mechanisms of Mg, especially the activation of pyramidal II slip, are dependent on the *loading direction, sample size, and loading rate*. To provide valuable insights for material design, experimental conditions must be selected carefully. In this investigation, high strain rate compression testing, of 15 μm micropillars, was combined with postmortem TEM characterization to analyze the deformation mechanisms of Mg during c-axis compression. The mechanical properties, deformation mechanisms, and their rate dependency, including the active slip systems and dislocation structures, present at specific loading conditions, were identified.

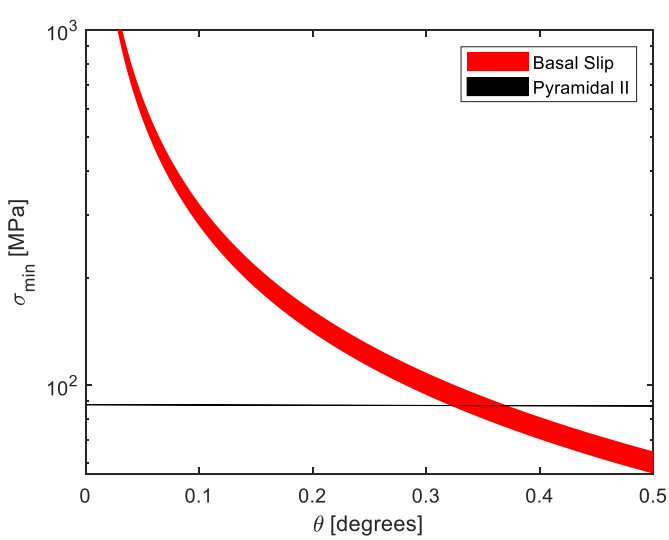

Fig. 1. Minimum normal stress, required for activation of basal slip and pyramidal II slip, as a function of misalignment between the loading direction and c-axis. The minimum stress, at a given misalignment, is given in a range because the exact value is dependent on details of the loading direction.

2. Material and experimental procedures

A single crystal Mg substrate of (0 0 0 1) orientation (grown by the modified Bridgman method) was purchased from MTI Corporation. Micropillars were prepared using laser milling followed by focused ion beam (FIB) polishing with an FEI Helios Nanolab microscope with a Ga + ion beam operated at 30 kV, as described in (Lin et al., 2021). It is reported (Byer and Ramesh, 2013) that when the diameter of a Mg pillar falls below 10 μm, its mechanical properties deviates from bulk Mg since the deformation mechanisms are dominated by exhaustion hardening (Senger et al., 2008; Benzerga, 2008; Rao et al., 2008; Tang et al., 2008) or source-truncation hardening (Parthasarathy et al., 2007). Hence, the diameter of pillars in this study is chosen to be 15 μm to avoid such mechanism and to better represent bulk behavior. The aspect ratio is 3:1 to avoid edge effect, i.e., frictional forces and confinement, and bending instability. The top surface of the pillars is polished edge-on using the FIB to reduce its roughness and potential stress concentration points. A representative pillar is shown in Fig. 2 (a).

Micropillar compression tests were carried out *in situ* in a SEM using a micromechanical testing system (Guillonneau et al., 2018). Three strain rates were explored, namely $10^{-3}/s$, $100/s$ and $250/s$. The quasi-static tests were displacement-controlled while the setup and data reduction method for high-strain tests are detailed in (Lin et al., 2021). In quasi-static tests, force is measured by a load cell, which has inherent compliance. A feedback control loop is implemented to compensate for that to achieve true displacement control. In high strain rate tests, the samples are situated on a virtually rigid substrate, and force is measured using a piezo tube, which is much stiffer than the pillars under

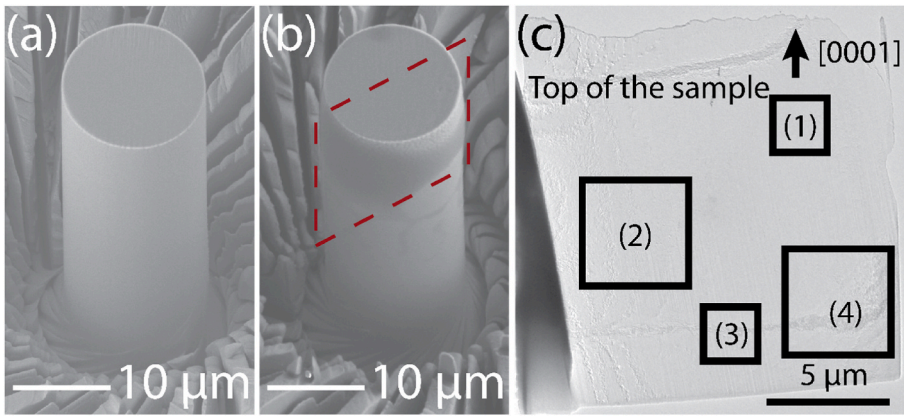

Fig. 2. SEM images of a representative Mg pillar: (a) as prepared and (b) after compression at a strain rate of 250/s up to 6% strain. TEM samples were extracted from the center top of the pillars, dashed lines in (b). (c) SEM image of a TEM sample. Numbers in (c) are labels to designate different locations where TEM characterization was carried out.

compression. Therefore, the deformation of the piezo tube is negligible compared to the pillars, and the tests can be deemed as displacement controlled. The sink-in effect of the substrate was accounted for in the force-displacement curves by applying the Sneddon method (Sneddon, 1965). The engineering stress-strain curves were obtained from the corrected force-displacement response and undeformed micropillar dimensions.

TEM characterization was performed on pillars from the as received, strained at $10^{-3}/s$, and strained at $250/s$ conditions. TEM samples were taken from the top one-third of the pillars at the centerline parallel to a $\{\bar{1}010\}$ plane, as shown in Fig. 2 (b). The TEM foils were prepared in an FEI Helios 600 FIB microscope. Thin samples were carved from micropillars and thinned to approximately 300 nm. The samples were finally polished at 5 kV with an ion beam current of 15 pA to minimize the Ga + ion beam damage (Wang et al., 2020). To mitigate the effect of surface oxide layers, plasma ion milling was performed immediately before TEM imaging at 200 eV for 30 s on each side of a sample with the beam inclined at 8° from the surface. A representative TEM sample is shown in Fig. 2 (c). An FEI Talos F200X (S)TEM operated at 200 kV was used for the TEM investigations.

3. Results

Representative engineering stress-strain curves for samples tested at $10^{-3}/s$, $100/s$ and $250/s$ are shown in Fig. 3a. Repeatability of the measurements is illustrated in Fig. 3b. The measured mechanical properties, (yield stress, hardening slope, and flow stress at 3% strain) are summarized in Table 1. As expected, the yield stress, obtained at a 0.2% offset, increases as strain rate increases. Beyond 1% strain, the flow stress is consistently higher in the high strain rate tests as compared to the quasi-static tests. The difference is less significant when the strain rate is 100/s. The post yield hardening rate is very similar at all tested strain rates. Notably, the hardening rate of the sample tested at 250/s shows a decrease beyond 4% strain, which could be attributed in part to errors in data analysis, due to the testing system dynamics, (Lin et al., 2021) and in part to the fact that at later stages of deformation, the plastically deformed crystals undergo small rotations with local reorientation of the basal planes potentially leading to more prominent basal

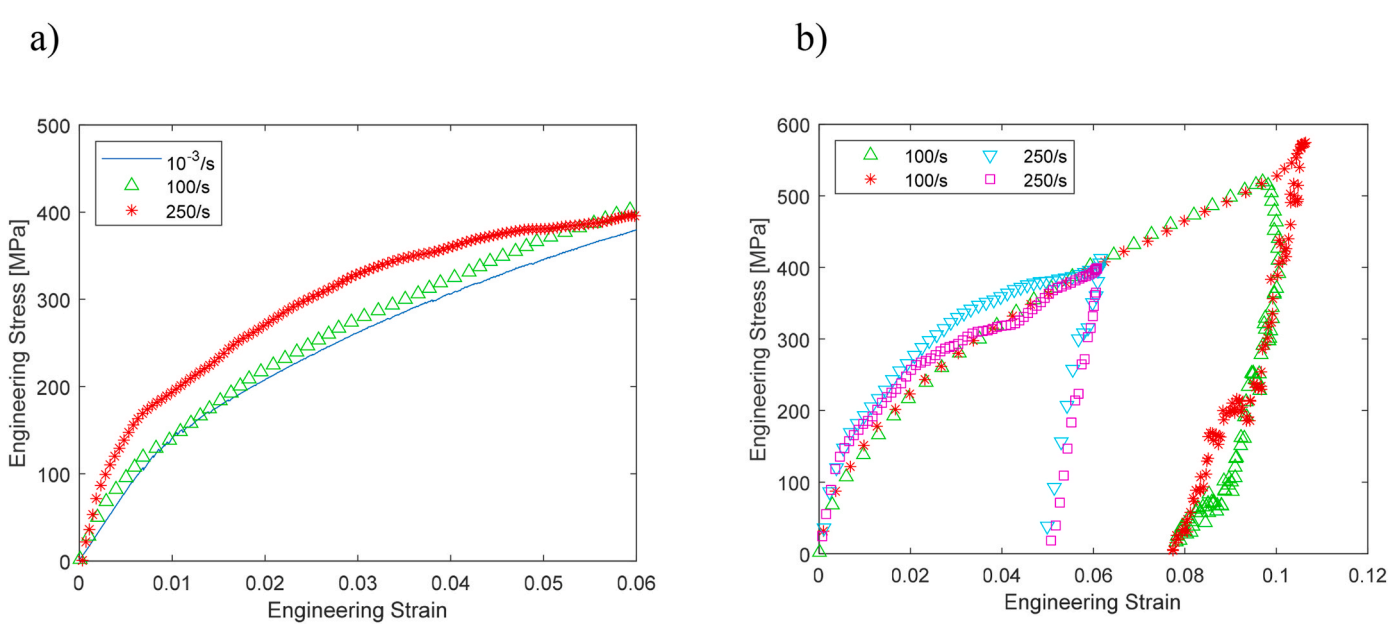

Fig. 3. a) Representative engineering stress-strain curves for micropillars tested at strain rates of $10^{-3}/s$, $100/s$, and $250/s$. b) High-strain rate measurement repeatability. The unloading moduli match the elastic modulus of Mg along c-axis (51 GPa). Micropillars compressed at 100/s were unloaded at about 10% strain while micropillars compressed at 250/s were loaded up to about 6% strain before unloading.

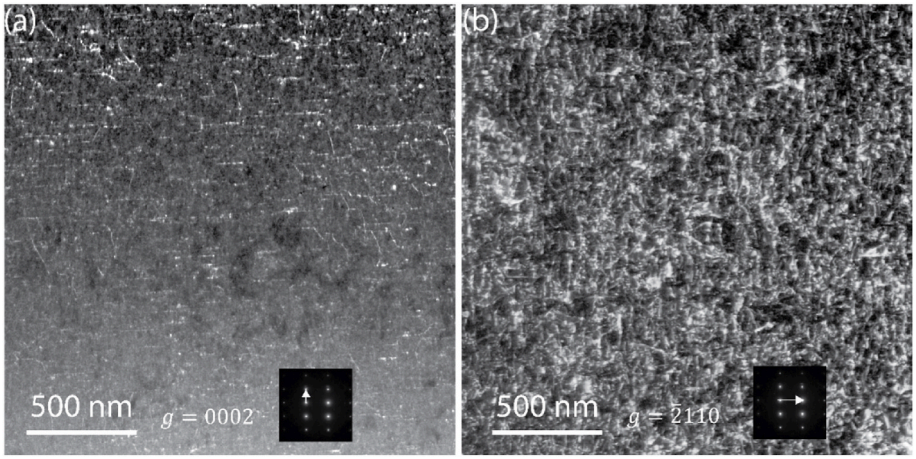

Fig. 4. Strong beam dark field TEM images of a sample tested at $10^{-3}/s$ taken using (a) $g = 0002$ and (b) $g = \bar{2}110$.

Table 1
Mechanical properties obtained from measured stress-strain curves.

Condition	Yield stress [MPa]	Post-yield slope [GPa]	Flow stress at 3% strain [MPa]
$10^{-3}/s$	106	5.9	262
$100/s$	120	6.6	276
$250/s$	154	6.9	329

slip activity (see for example Fig. 2c in Lilleodden, 2010).

Postmortem SEM imaging was carried out on the tested pillars. Fig. 2 (b) shows a pillar tested at 250/s up to 6% strain, where there is no shear offset (slip on a localized region of the sample) typically associated with micropillar compression tests (see for example Fig. 2c in (Lilleodden, 2010) or Fig. 4 in Byer and Ramesh, 2013). Instead, the Mg micropillar shows an expansion in the diameter consistent with a uniform compressive strain. Micropillars tested at strain rates of $10^{-3}/s$ and $100/s$, up to 6% strain, also show no sign of basal slip activation or twinning induced fracture.

TEM imaging was carried out on samples taken from micropillars tested at strain rates of $10^{-3}/s$ and $250/s$. From the $g \bullet b = 0$ invisibility criterion, (Williams and Carter, 2009) where g is the diffraction vector and b is the Burgers vector of a dislocation, <a> type dislocations are invisible when $g = 0002$ and <c> type dislocations are invisible when $g = \bar{2}110$. <a+c> dislocations are visible under either g vector condition. Such visibility conditions enable dislocation types to be distinguished as summarized in Table 2. TEM samples were prepared from one $\{\bar{1}010\}$ plane, as the two g conditions could be reached with little tilt.

Two strong beam dark field TEM images, for a sample tested at $10^{-3}/s$ up to 6% strain, are shown in Fig. 4. Both images were taken from the same region. Dislocations are visible under both $g = 0002$, in Fig. 4 (a), and $g = \bar{2}110$, in Fig. 4 (b). This implies the presence of <a+c> type dislocations. However, when $g = 0002$, Fig. 4 (b), a much higher density of dislocations is observed than when $g = \bar{2}110$, Fig. 4 (a). Since both <a> and <a+c> type dislocations are visible in Fig. 4 (b), the higher dislocation density observed under the $g = \bar{2}110$ condition implies the presence of <a> type dislocations with a density comparable to the <a+c> type. In Fig. 4 (a), the <a+c> type dislocations appear as traces with short straight segments bound in the basal plane, while most dislocations in Fig. 4 (b) appear to form a complicated network without preferential orientation, which is characteristic of basal slip dislocations.

Table 2
Visibility conditions for dislocations with different Burgers vectors at selected diffraction conditions.

g	$<a>$	$<c>$	$<a+c>$
0002	invisible	visible	visible
$\bar{2}110$	visible	invisible	visible
$\bar{1}010$	–	invisible	–

Dislocation activity at different locations of a sample tested at 250/s, as indicated in Fig. 2 (c), is captured in the bright field TEM images shown in Fig. 5. All locations exhibit high dislocation densities. Furthermore, this high strain rate sample, although loaded up to the same 6% strain, has a much higher amount of residual stress than the one loaded at $10^{-3}/s$. This is evident from the presence of bend contours in the TEM images. Indeed, during TEM sample preparation, the foil warped significantly suggesting a complex dislocation network and high internal stresses. In contrast, the quasi-statically loaded one remained relatively flat, see Fig. 4.

Dark field TEM images, taken with $g = \bar{2}110$ and corresponding to the images shown in Fig. 5, are shown in Fig. 6. Comparing Figs. 5 and 6 reveals that many of the observed dislocations are of <a+c> type, as they are overserved when $g = 0002$ and $g = \bar{2}110$, respectively. A more detailed analysis of individual dislocation segments, confirming the abundance of <a+c> type dislocations, is shown in Fig. 7. While in Fig. 4, <a> type dislocations are present in significant amount in the quasi-statically loaded sample, Figs. 5 and 6 show equally high number of dislocations, suggesting the predominance of <a+c> type dislocations in the sample loaded at high stain rate. While many dislocation lines are bound in the basal plane traces, long zig-zag segments out of the basal planes are also present.

Dislocation densities were measured from the TEM images shown in Fig. 8 for as prepared and tested samples, the later at 250/s and up to 6% strain. The projected length l_p of dislocation lines in the images was measured manually and the dislocation density calculated using the formula $= l/At$, where $l = 4l_p/\pi$ (Bailey and Hirsch, 1960). The thickness of the foils, t, was measured using electron energy loss spectroscopy (see Fig. 8c). The <a> type dislocations form a complex network making the quantification of dislocation density very challenging. Following (Dixit et al., 2015), only the density of <a+c> type dislocations were measured, as this has been suggested to be the reason for the high degree of strain hardening (Obara et al., 1973). The apparent dislocation densities are $2.4 \times 10^{12}/m^2$ and $2.0 \times 10^{13}/m^2$, respectively.

4. Discussion

4.1. Strain rate effects on the mechanical properties and strain hardening

We begin by noting that the stress-strain behavior at the initial stages of loading shows some rate dependency (Fig. 3). However, it is known that in micropillar compression experiments, the initial slope of the

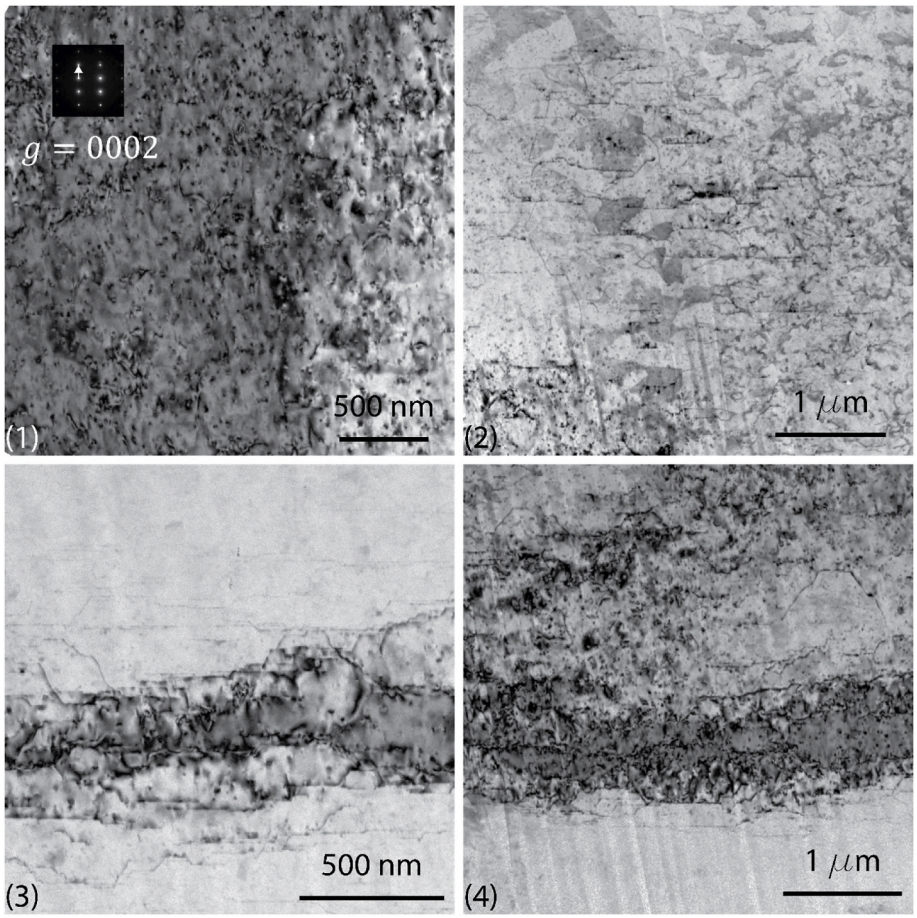

Fig. 5. Bright field TEM images showing dislocations at different locations (indicated by the numbering provided in Fig. 2(c)) on the sample tested at 250/s. These TEM images are under the diffraction condition of $\boldsymbol{g} = \mathbf{0002}$, so the visible dislocations have a Burgers vector with a <c> component based on the dislocation extinction criterion, and they may be <c> or <a+c> dislocations.

stress-strain curves rarely matches the theoretical Young's modulus due to load misalignment, nonuniform contact of the punch, etc. The feature is also observed in high-strain-rate compression tests, see e.g., Li (2011) likely due to the significant misalignment (around 10°) and the nonequilibrium conditions present at the early stages of deformation in Hopkinson bar experiments. In contrast, when the stress-strain behavior is well into the plastic regime, the mechanical behavior of single crystal Mg, clearly exhibits limited rate sensitive up to strain rates of 250/s, in agreement with previous studies performed on bulk single crystal Mg (Li, 2011, 2013).

Another observation, is that both quasi-static and high-strain rate micropillar testing reveal a high rate of hardening consistent with the strength dependent basal dissociation of <a+c> dislocations into immobile dislocations, as proposed by Curtin in 2015 (Wu and Curtin, 2015), which act as "forest dislocations," leading to the rapid strain hardening observed in all the experiments here reported.

The basal dissociation process is a kinetic process with a characteristic time, hence, sliding of <a+c> dislocations can occur over certain distances before dissociation into immobile dislocations. This feature has several implications, on one hand, there is size dependence manifested by the diameter of the pillars or the grain size in bulk Mg. In submicron pillars and more interesting in pillars with diameters as large as 15 μm, as here reported, high ductility resulting from <a+c> dislocations is achieved in the absence of twining as in bulk. On the other hand, higher stresses achieved during the initial loading stage in the 250/s experiment, increases the probability of activation of <a+c> type dislocations. This appears to be less pronounced at 100/s. Indeed, MD reveals that the transition of easy glide pyramidal II edge dislocations is very complex and stress dependent (see Fig. 1 in Wu and Curtin, 2015). As stated by Curtin, the transition into the final state is preceded by an intermediate state where a partial <a> is nucleated on the basal plane. This partial <a> can then glide in the presence of a shear stress. The glide behavior of the various dislocations under applied resolved shear stress is also very dependent on stress magnitude, making for a variety of plasticity scenarios. At later stages, even as the stress level continues to rise, the plastically deformed crystals undergo small rotations, with local reorientation of the basal planes, leading to more prominent basal slip activity. Due to its extremely small CRSS, basal slip will eventually dominate the hardening behavior, which would explain the observed rate insensitivity at higher stress levels. This is also evident from the TEM observation, as discussed below.

4.2. Strain rate effect on deformation mechanisms and dislocation types

While both <a> and <a+c> type dislocations are present in Mg deformed at both quasi-static and high strain rates, the relative amounts are very different. In the sample loaded at a quasi-static strain rate, the <a+c> segments are short, and the <a> type dislocations appear in mass and outnumber the former. This is evident in Fig. 4 (b), where both <a> and <a+c> dislocation types are visible, and the total dislocation density is higher than in Fig. 4 (a) in which only <a+c> type is visible. On the contrary, in the sample loaded at high strain rate, most of the dislocations are of <a+c> type, as shown in Figs. 5 and 6, with a comparably high density of dislocations. The existence of <a> type dislocations is also evident, yet they are not the dominant species.

As shown in Fig. 1, a misalignment of a fraction of a degree is enough

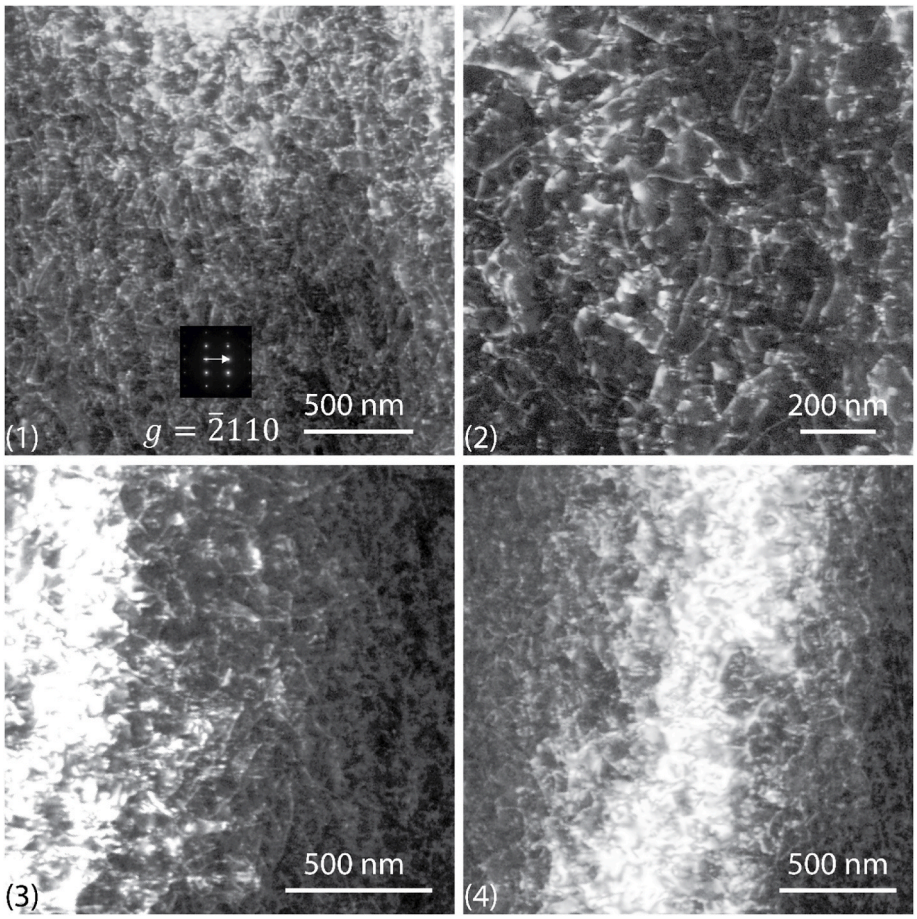

Fig. 6. Dark field TEM images under the diffraction condition of $\boldsymbol{g} = \bar{\mathbf{2}}\mathbf{110}$ taken at the locations depicted in Fig. 2 (c). Under this diffraction condition, dislocations with <a> and <a+c> components are visible.

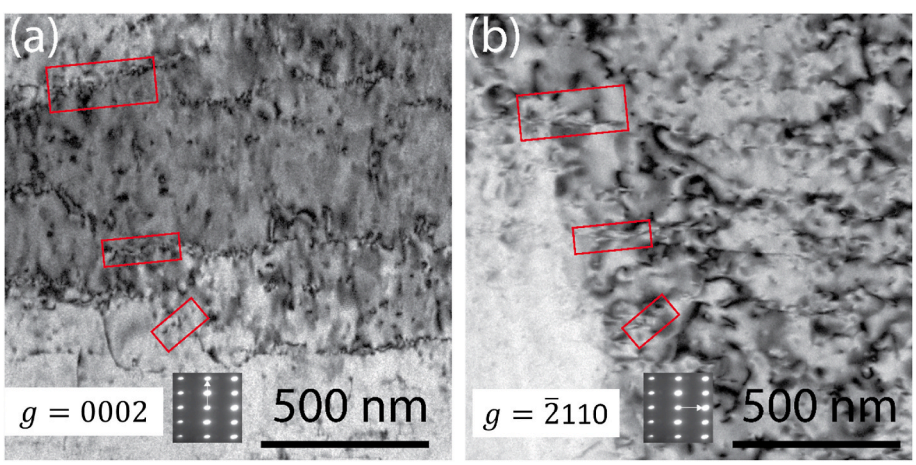

Fig. 7. Bright field TEM images taken under diffraction conditions of (a) $g = 0002$ and (b) $g = \bar{2}110$. Based on the $g \bullet b = 0$ invisibility criterion, only <a+c> type dislocations could be visible under both conditions (see Table 1). The rectangles in both images highlight the same dislocations. The dislocation lines appear along the basal plane traces, indicating their confinements to the basal planes, which was also reported in (Obara et al., 1973) and (Syed et al., 2012).

for the activation of basal slip. This issue might not be significant in nano- and even micro-scale samples of just a few microns. At such length scales, few initial dislocations are available for slip and multiplication. Hence, the mechanical properties are controlled by "dislocation starvation" (Tang et al., 2008; Greer et al., 2005) and other types of dislocation activities (Senger et al., 2008; Benzerga, 2008; Rao et al., 2008; Tang et al., 2008; Greer et al., 2008) where the free surface of the samples plays a significant role. However, as the size of the sample grows towards the bulk, as in this study, the boundary effect disappears. Given the extremely low CRSS of basal slip in Mg, their activity is expected in large samples, as is the case in this study.

At quasi-static strain rates, basal slip of partial <a> dislocations resulting from the transition of easy glide pyramidal II dislocations, may play a considerable role in the overall mechanical behavior. Indeed, in

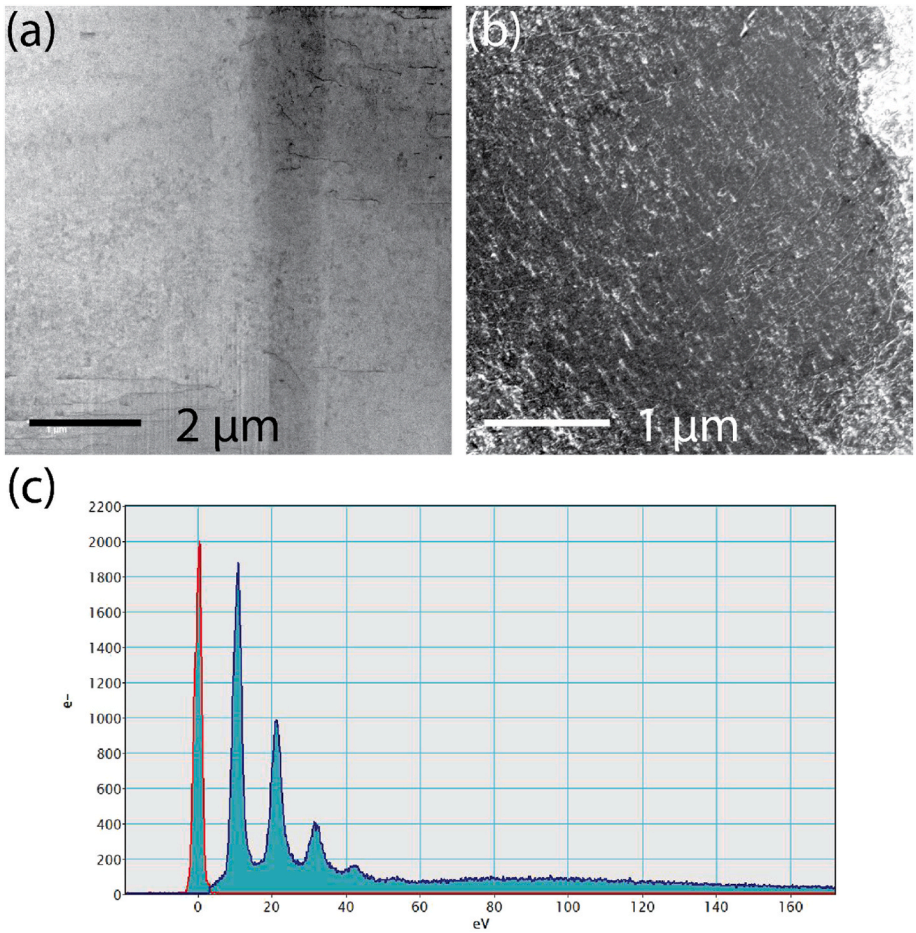

Fig. 8. Characterization of dislocation density for pillars (a) as-prepared and (b) tested at strain rate of 250/s up to 6% strain. The total length of dislocations lines is measured and divided by the volume of the sample, which is the product of the view area and the thickness of the sample, measured by means of electron energy loss spectroscopy (EELS). The EELS signal is shown in (c), which corresponds to a thickness of 300 nm that equals about 1.92 inelastic mean free paths. The EELS data was collected in STEM mode with a convergence semi-angle of 21 mrad and collection semi-angle of 41.7 mrad. The dispersion was 0.1 eV/channel. The sample thickness was estimated by using the log-ratio method. The mean free path, lambda, was estimated as 155 nm based on the mean atomic number.

(Lilleodden, 2010), a Mg pillar compressed along the c-axis shows instability at ~6% strain, in the form of complete shear-off of the inner section along the basal planes. Basal slips are also present in the sample loaded at high strain rate. However, their role appears less significant than in the quasi-static case.

Though deformation twinning is a mechanism that can accommodate deformation along the c-axis in HCP metals, the typical $\{10\bar{1}2\}$ twin can only lead to expansion along the c-axis (Barnett, 2007a, 2007b). Alternatively, compression twinning (i.e., $\{10\bar{1}1\}$ or $\{10\bar{1}3\}$ twins) may accommodate c-axis compression (Barnett, 2007b). However, *no evidence of twins is observed in the TEM micrographs*. Thus, while some strain may be accommodated through basal slip it falls short of the imposed strain. The difference must be made up by <a+c> type dislocations. Second, as the imposed strain is not mediated through dislocation plasticity efficiently, elastic strain and stress build up lead to a higher stress level compared to quasi-static loading, as shown in Fig. 2, which promotes further activation of the pyramidal II slip system. Third, the glide of <a+c> type dislocations are enhanced by higher stresses present in the sample loaded at high strain rate (see Fig. 2 in Wu and Curtin, 2015), also evident by the bend contours observed in TEM images and the significant warping of the TEM sample. This is likely due to the easy double cross-slip (Obara et al., 1973) and the formation of dipoles (Liu et al., 2019) of <a+c> type dislocations.

Another observation regarding the dislocation morphology in the sample loaded at high strain rate is that dislocations are distributed throughout the sample. This enhancement of plasticity appears to delay fracture. While there is a significant variability in the reported strain that Mg can achieve before fracture, for bulk samples tested at room temperature, the fracture strain is usually reported to be 4–6%, (Obara et al., 1973; Wonsiewicz, 1966; Li, 2011) with some as low as 1% (Syed et al., 2012). Micropillars usually achieve higher strain before fracture, which is attributed to fewer defects in the smaller sample volume. In this study, pillars tested at high strain rate show no sign of fracture up to 10% strain.

4.3. *Strain rate effect on the mobility of <a+c> type dislocations and plasticity*

The <a+c> straight segments lying parallel to the intersection of pyramidal and basal planes, see Fig. 9, are of edge type. Their formation has been attributed to the low mobility of edge dislocations, (Obara et al., 1973) formation of sessile dislocation, (Li et al., 2017) dissociation of <a+c> dislocations into partials, (Wu and Curtin, 2015) and the formation of dislocation dipoles (Liu et al., 2019). This low mobility limits the plasticity of Mg along the c-axis to as low as 1% (Syed et al., 2012). While in the quasi-statically loaded sample, we found most of the <a+c> type dislocations bound in the intersection of pyramidal and basal planes, the sample loaded at high strain rate shows a significant amount of <a+c> type dislocations having long screw type segments. Fig. 9(a) and (b) are two TEM images taken at $g = 0002$ and $g = \bar{2}110$,

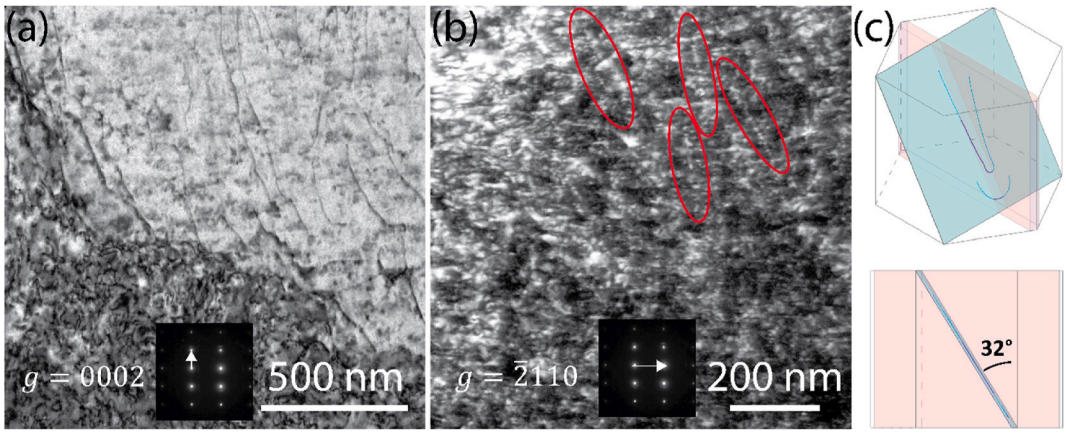

Fig. 9. (a) Bright field TEM images taken at $g = 0002$ and (b) dark field TEM image taken at $g = \bar{2}110$ of a sample tested at 250/s. (c) Schematic showing the relative position of the TEM sample and one of the $\{11\bar{2}2\}$ planes with two representative dislocation lines on this slip plane. Short edge segments on basal planes, observed at quasi-static strain rates (Fig. 4 (a)), and long screw segments, observed at high strain rates (images a and b).

showing the dislocations in a sample tested at 250/s. The invisibility conditions confirm that the <a+c> type nature of the dislocations. Unlike those <a+c> type dislocations bound in the traces of the basal plane, the ones shown here extend a few microns at an angle with respect to the basal planes, Fig. 9 (c).

To understand the nature of these long dislocation segments, it is helpful to visualize the relative position of the TEM sample and the slip plane on which dislocation glides. Typically, long dislocation segments can only be found when the TEM sample is prepared along the slip planes of dislocations because of the 2-D nature of the TEM sample foil. One exception is when the dislocations lie within the intersection of the TEM foil and the slip plane. Fig. 9 (c) is a schematic showing a unit cell of the hexagonal close packed crystal, one of the $\{11\bar{2}2\}$ planes and the TEM sample, which is on the $\{\bar{1}010\}$ plane. Since the thickness of the TEM foil is approximately 300 nm, the <a+c> dislocations must be of screw type (or mostly), to appear as long segments in the TEM foils. This is illustrated by the two representative dislocation lines in the slip plane, with the portion within the TEM foil colored in purple. The longer segment is parallel to the Burgers vector <a+c>, suggesting the screw type nature of the dislocation. The edge type, on the other hand, intersects with the TEM foil by a small length.

This geometric relationship is also obvious in the orientation of the dislocation lines in the TEM images. When the electron beam is almost perpendicular to the TEM sample, the screw type with long segments makes an angle of about 32° with the c-axis, as shown in Fig. 9 (c). TEM images in Fig. 9(a) and (b) show exactly this geometric relationship, corroborating that the slip plane is $\{11\bar{2}2\}$.

The presence of long, mobile screw type dislocations in the sample tested at high strain rate, is due to the higher stress achieved by c-axis compressed samples at the early stage of the loading. This increased dislocation activity is evident by the presence of numerous bend contours in the TEM images. The higher activation of the <a+c> type dislocation may be responsible for the higher amount of plasticity in the sample tested at high strain rates, *which exceeded 10% without signs of facture*. This significant amount of plasticity was previously observed only in nanopillars (Liu et al., 2019) with diameters less than 1 μm, where the plasticity is achieved through a combination of defect-free state of the sample and a large surface-to-volume ratio for dislocation annihilation.

5. Conclusions

In this study, we investigated the mechanical properties and deformation mechanisms of single-crystal Mg micropillars compressed along the c-axis at quasi-static strain rate and strain rates of up to 250/s. Micropillars 15 μm in diameter were investigated to capture more of the bulk properties of the material rather than small scale size effects associated to dislocation starvation, as observed in micropillars of 1 μm in diameter or smaller. The findings reported here, including achievement of large plastic deformation, *in the absence of twining and fracture*, for both quasi-static and high strain rate deformations are relevant to the design of lightweight materials used in transportation systems. It hints at the use of Mg with grain sizes of just a few microns to preserve ductility. Likewise, they represent a unique set of experimental data that the materials science community could use in exploring atomistic mechanisms of plasticity in the presence of strain rates, as well as the validation of discrete dislocation dynamics (DDD) formulations employed in multiscale design of materials.

Key findings revealed by the measured stress-strain curves and TEM observation are:

- At high deformation rates, <a+c> type pyramidal II slip is the primary deformation mechanism of plasticity *with no observation of deformation twining.*
- Activation of highly mobile <a+c> type dislocation appears responsible for the higher amount of plasticity in samples tested at high strain rates, *exceeding 10% strain without signs of facture.*
- The contribution of <a> type basal slip is not negligible, especially at a quasi-static strain rate. For the case of high strain rates, their contribution appears significant at large deformations leading to a flow stress similar to the one measured quasi-statically.
- At high strain rates, <a+c> type dislocations have longer segments and their screw components are very mobile, compared to those present at quasi-static strain rates. This feature appears to result in an increase in sample ductility.

CRediT authorship contribution statement

Z. Lin: Formal analysis, Investigation, Methodology, Visualization, Writing – original draft. **D.J. Magagnosc:** Formal analysis, Methodology, Writing – review & editing. **J. Wen:** Formal analysis, Methodology, Writing – review & editing. **X. Hu:** Formal analysis, Methodology, Writing – review & editing. **H.D. Espinosa:** Conceptualization, Formal analysis, Funding acquisition, Supervision, Writing – review & editing.

Declaration of competing interest

The authors declare the following financial interests/personal relationships which may be considered as potential competing interests: Horacio D. Espinosa reports financial support was provided by

Northwestern University.

Data availability

Data will be made available on request.

Acknowledgements

H. D. Espinosa gratefully acknowledges financial support from DEVCOM Army Research Lab through award No. W911NF1220022. Use of the Center for Nanoscale Materials, an Office of Science user facility, was supported by the U.S. Department of Energy, Office of Science, Office of Basic Energy Sciences, under Contract No. DE-AC02-06CH11357.

References

Ando, S., Tsushida, M., Kitahara, H., 2010. Deformation behavior of magnesium single crystal in c -Axis compression and a -Axis tension. Mater. Sci. Forum 654–656, 699–702.
Bailey, J.E., Hirsch, P.B., 1960. The dislocation distribution, flow stress, and stored energy in cold-worked polycrystalline silver. Phil. Mag. 5 (53), 485–497.
Barnett, M.R., 2007a. Twinning and the ductility of magnesium alloys: Part I: "Tension" twins. Mater. Sci. Eng., A 464 (1), 1–7.
Barnett, M.R., 2007b. Twinning and the ductility of magnesium alloys: Part II. "Contraction" twins. Mater. Sci. Eng., A 464 (1), 8–16.
Benzerga, A.A., 2008. An analysis of exhaustion hardening in micron-scale plasticity. Int. J. Plast. 24 (7), 1128–1157.
Burke, E.C., Hibbard, W.R., 1952. Plastic deformation of magnesium single crystals. JOM 4 (3), 295–303.
Byer, C.M., Ramesh, K.T., 2013. Effects of the initial dislocation density on size effects in single-crystal magnesium. Acta Mater. 61 (10), 3808–3818.
Byer, C.M., Li, B., Cao, B., Ramesh, K.T., 2010. Microcompression of single-crystal magnesium. Scripta Mater. 62 (8), 536–539.
Chapuis, A., Driver, J.H., 2011. Temperature dependency of slip and twinning in plane strain compressed magnesium single crystals. Acta Mater. 59 (5), 1986–1994.
Conrad, H., Robertson, W.D., 1957. Effect of temperature on the flow stress and strain-hardening coefficient of magnesium single crystals. JOM 9 (4), 503–512.
Dixit, N., Xie, K.Y., Hemker, K.J., Ramesh, K.T., 2015. Microstructural evolution of pure magnesium under high strain rate loading. Acta Mater. 87, 56–67.
Dziubińska, A., Gontarz, A., Dziubiński, M., Barszcz, M., 2016. The forming of magnesium alloy forgings for aircraft and automotive applications. Advances in Science and Technology Research Journal 10 (31), 158–168.
Flynn, P.W., Mote, J., Dorn, J.E., 1961. On the thermally activated mechanism of prismatic slip in magnesium single crystals. T Metall Soc Aime 221 (6), 1148–1154.
Greer, J.R., Oliver, W.C., Nix, W.D., 2005. Size dependence of mechanical properties of gold at the micron scale in the absence of strain gradients. Acta Mater. 53 (6), 1821–1830.
Greer, J.R., Weinberger, C.R., Cai, W., 2008. Comparing the strength of f.c.c. and b.c.c. sub-micrometer pillars: compression experiments and dislocation dynamics simulations. Mater. Sci. Eng., A 493 (1–2), 21–25.
Guillonneau, G., Mieszala, M., Wehrs, J., Schwiedrzik, J., Grop, S., Frey, D., Philippe, L., Breguet, J.-M., Michler, J., Wheeler, J.M., 2018. Nanomechanical testing at high strain rates: new instrumentation for nanoindentation and microcompression. Mater. Des. 148, 39–48.
Joost, W.J., Krajewski, P.E., 2017. Towards magnesium alloys for high-volume automotive applications. Scripta Mater. 128, 107–112.
Klaumünzer, D., Hernandez, J.V., Yi, S., Letzig, D., Kim, S.-h., Kim, J.J., Seo, M.H., Ahn, K., 2019. Magnesium process and alloy development for applications in the automotive industry. In: The Minerals, Metals & Materials Series. Springer International Publishing, pp. 15–20.
Li, Q., 2011. Dynamic mechanical response of magnesium single crystal under compression loading: experiments, model, and simulations. J. Appl. Phys. 109 (10).
Li, Q., 2013. Microstructure and deformation mechanism of 0001 magnesium single crystal subjected to quasistatic and high-strain-rate compressiveloadings. Mater. Sci. Eng., A 568, 96–101.
Li, B., Ma, E., 2009. Pyramidal slip in magnesium: dislocations and stacking fault on the {1011} plane. Phil. Mag. 89 (14), 1223–1235.
Li, B., Zhang, Q.W., Mathaudhu, S.N., 2017. Basal-pyramidal dislocation lock in deformed magnesium. Scripta Mater. 134, 37–41.
Lilleodden, E., 2010. Microcompression study of Mg (0001) single crystal. Scripta Mater. 62 (8), 532–535.
Lin, Z., Magagnosc, D.J., Wen, J., Oh, C.S., Kim, S.M., Espinosa, H.D., 2021. In-situ SEM high strain rate testing of large diameter micropillars followed by TEM and EBSD postmortem analysis. Exp. Mech. 61 (5), 739–752.
Liu, B.-Y., Liu, F., Yang, N., Zhai, X.-B., Zhang, L., Yang, Y., Li, B., Li, J., Ma, E., Nie, J.-F., Shan, Z.-W., 2019. Large plasticity in magnesium mediated by pyramidal dislocations. Science 365 (6448), 73–75.
Mises, R.V., 1928. Mechanik der plastischen Formänderung von Kristallen. ZAMM - Zeitschrift für Angewandte Mathematik und Mechanik 8 (3), 161–185.
Obara, T., Yoshinga, H., Morozumi, S., 1973. {112¯2}⟨23⟩ Slip system in magnesium. Acta Metall. 21 (7), 845–853.
Parthasarathy, T.A., Rao, S.I., Dimiduk, D.M., Uchic, M.D., Trinkle, D.R., 2007. Contribution to size effect of yield strength from the stochastics of dislocation source lengths in finite samples. Scripta Mater. 56 (4), 313–316.
Quimby, R., Mote, J., Dorn, J., 1962. Yield point phenomena in magnesium-lithium single crystals. Am. Soc. Metals, Trans. Quart. 55.
Rao, S.I., Dimiduk, D.M., Parthasarathy, T.A., Uchic, M.D., Tang, M., Woodward, C., 2008. Athermal mechanisms of size-dependent crystal flow gleaned from three-dimensional discrete dislocation simulations. Acta Mater. 56 (13), 3245–3259.
Reed-Hill, R.E., Robertson, W.D., 1957a. Deformation of magnesium single crystals by nonbasal slip. JOM 9 (4), 496–502.
Reed-Hill, R.E., Robertson, W.D., 1957b. Additional modes of deformation twinning in magnesium. Acta Metall. 5 (12), 717–727.
Reedhill, R.E., Robertson, W.D., 1958. Pyramidal slip in magnesium. T Am I Min Met Eng 212, 256–259.
Roberts, C.S., 1960. Magnesium and its Alloys. Wiley, New York, p. 230.
Senger, J., Weygand, D., Gumbsch, P., Kraft, O., 2008. Discrete dislocation simulations of the plasticity of micro-pillars under uniaxial loading. Scripta Mater. 58 (7), 587–590.
Sneddon, I.N., 1965. The relation between load and penetration in the axisymmetric boussinesq problem for a punch of arbitrary profile. Int. J. Eng. Sci. 3 (1), 47–57.
Stohr, J.F., Poirier, J.P., 1972. Etude en microscopie electronique du glissement pyramidal {1122} ⟨1123⟩ dans le magnesium. Phil. Mag. 25 (6), 1313–1329.
Syed, B., Geng, J., Mishra, R.K., Kumar, K.S., 2012. [0001] Compression response at room temperature of single-crystal magnesium. Scripta Mater. 67 (7–8), 700–703.
Tang, H., Schwarz, K.W., Espinosa, H.D., 2008. Dislocation-source shutdown and the plastic behavior of single-crystal micropillars. Phys. Rev. Lett. 100 (18).
Taylor, G.I., 1938. Plastic strain in metals. J I Met 62, 307–324.
Wang, J., Molina-Aldareguía, J.M., Llorca, J., 2020. Effect of Al content on the critical resolved shear stress for twin nucleation and growth in Mg alloys. Acta Mater. 188, 215–227.
Williams, D.B., Carter, C.B., 2009. The transmission electron microscope. In: Transmission Electron Microscopy. Springer US, pp. 3–22.
Wonsiewicz, B.C., 1966. Plasticity of Magnesium Crystals. Massachusetts Institute of Technology.
Wu, Z., Curtin, W.A., 2015. The origins of high hardening and low ductility in magnesium. Nature 526 (7571), 62–67.
Wu, Z., Ahmad, R., Yin, B., Sandlöbes, S., Curtin, W.A., 2018. Mechanistic origin and prediction of enhanced ductility in magnesium alloys. Science 359 (6374), 447–452.
Yoshinaga, H., Horiuchi, R., 1963. Deformation mechanisms in magnesium single crystals compressed in the direction parallel to hexagonal Axis. Transactions of the Japan Institute of Metals 4 (1), 1–8.
Yoshinaga, H., Obara, T., Morozumi, S., 1973. Twinning deformation in magnesium compressed along the C-axis. Mater. Sci. Eng. 12 (5–6), 255–264.
Yu, Q., Qi, L., Chen, K., Mishra, R.K., Li, J., Minor, A.M., 2012. The nanostructured origin of deformation twinning. Nano Lett. 12 (2), 887–892.